Thermally induced metal-to-insulator transition in NbO_2 thin films: Modulation of the transition temperature by epitaxial strain

Toyanath Joshi,* Eli Cirino, Sophie A. Morley, and David Lederman
Department of Physics, University of California, Santa Cruz, California 95064, USA

(Received 25 August 2019; revised manuscript received 28 October 2019; published 16 December 2019)

Modification of the carrier dynamics in correlated oxide systems via epitaxial strain is a promising pathway for the practical realization of energy-efficient electronic devices. Here we report on the thermally induced metal-to-insulator transition (MIT) of NbO_2 films grown on Al_2O_3 substrates and the modulation of the MIT temperature via epitaxial strain from the substrate. The metal-insulator transition temperature (T_{MIT}) increased from 910 to 1066 K with increasing strain. An ultrathin 3.9-nm film consisting of a single strained layer with minimal structural defects yielded a bulklike sharp transition. The substrate-induced strain offers another degree of freedom to improve device functionality of MIT materials.

DOI: 10.1103/PhysRevMaterials.3.124602

I. INTRODUCTION

The Mott insulator NbO_2 is the most investigated material for the implementation of neuromorphic computing [1–3]. By virtue of its thermally induced reversible metal-to-insulator transition (MIT) with threshold switching and current controlled–negative differential resistance, NbO_2 can emulate biological dendritic functionality. To date, the most prevalent application of this material is in current-switching elements in resistive random access memory (RRAM), where NbO_2 is layered with a memristor as a selector element in a cross-point structure [4–10] to trigger electrical signals that mimic the synaptic action which is the fundamental process of a neural network [1]. A memristor is a two-terminal nonvolatile memory device based on resistance switching and is a potential candidate for future computer memory elements [11]. These neuroinspired architectures have received much attention due to their energy efficiency, scalability, and speed in massively parallel computation applications [9].

Application of NbO_2 for RRAM is presently not feasible because of the large insulating-state leakage current reported to be greater than 10^{-5} A in devices made from amorphous and polycrystalline films [6,8,12–17]. The leakage current in nonstoichiometric NbO_x films originates from defects such as oxygen vacancies and grain boundaries [16]. In the case of stoichiometric epitaxial films, defects such as twin domain boundaries can be minimized by choosing appropriate substrates and/or growth conditions. Reduced leakage current not only helps to reduce heat dissipation while used in the device but also helps to increase the on-state to the off-state current ratio (I_{ON}/I_{OFF}) which is essential for enhanced device functionality. More systematic studies of epitaxial film structure-dependent thermally induced metal-to-insulator transitions in NbO_2 epitaxial thin films need to be made.

Bulk crystalline NbO_2 undergoes the structural change from a high-temperature rutile phase to a low-temperature tetragonal phase where the rutile and tetragonal phases correspond to the metallic and insulating phases, respectively [18–20]. The actual phase transition mechanism, however, is unclear and under debate. The most accepted mechanism relies on the stabilization of the low-temperature phase by Nb-Nb dimerization followed by a Peierls distortion along the c axis [19,21–24]. The high-temperature rutile structure has lattice parameters of $a_R = 4.846$ Å and $c_R = 3.032$ Å [21]. The axis transformation from the high-temperature rutile to the low-temperature tetragonal supercell (space group $I4_1/a$) is described by a change in the lattice constants $a_T = 2\sqrt{2}a_R = 13.702$ Å, and $c_T = 2\,c_R = 5.985$ Å, where the subscripts T and R refer to the tetragonal and rutile phases, respectively [19,21,25]. The metal-to-insulator transition temperature (T_{MIT}) in bulk NbO_2 has been reported to be in the vicinity of 1070 K [18,22,26–29]. This high T_{MIT} distinguishes NbO_2 from other MIT materials with structural phase changes, such as VO_2, making it more stable for use in electronic devices.

The conduction mechanism in the NbO_2 insulating state is controlled by small polaron hopping [18,30] between Nb^{4+} (in the $4d$ [1] configuration) ionic traps localized via pairing along the c axis stabilized by the lattice distortion. VO_2, which consists of a $3d$ [1] electron system, has a much lower T_{MIT} (340 K) than NbO_2. The reason for the higher T_{MIT} in NbO_2 is that the Nb $4d$-orbital energy states are more delocalized than the $3d$-orbital energy states in VO_2, with the $d_{\parallel} - e_g^{\pi}$ orbital energy splitting of NbO_2 being larger than in VO_2 by 0.3 eV [31]. The larger mass of the Nb atom with respect to V, on the other hand, may play a role in elevating the transition temperature. Shapiro *et al.* [22] found some evidence of a soft phonon mode in a neutron diffraction study but there has not been much investigation of the phase transition induced by phonon softening in NbO_2. Using VO_2 as a model [32–35], an extension along the c axis is expected to lower the Nb-O bond length, mainly along apical distances

*tojoshi@ucsc.edu

 ©2019 American Physical Society

in NbO_6 octahedra, which increases the metal-ligand overlap and thus increases the T_{MIT}. Therefore, modulation of the T_{MIT} in NbO_2 is feasible via substrate-induced epitaxial strain.

In this paper, we report direct measurements of the resistivity of epitaxial NbO_2 thin films near the metal-to-insulator transition temperature and modulation in T_{MIT} via epitaxial strain from the substrate. Our results provide insight toward the understanding of the phase change conduction mechanism in NbO_2 and its possible application in electronic devices.

II. EXPERIMENTAL DETAILS

NbO_2 epitaxial films were grown on single-crystal $Al_2O_3(0001)$ substrates (lattice parameters: $a = 0.476$ nm and $c = 1.30$ nm) using pulsed laser deposition (PLD) and a stoichiometric NbO_2 target. The samples were grown at 650 °C and 0.1 mTorr oxygen pressure or 2 mTorr O_2/Ar mixed pressure with 1% O_2. Ultrahigh-purity (UHP, 99.999%) grade O_2 and Ar gases were used. The film thickness was varied from 3.9 to 63.6 nm. Structural quality was examined *in situ* via reflection high-energy electron diffraction (RHEED) and by *ex situ* x-ray diffraction using a Rigaku SmartLab x-ray diffractometer with Cu $K\alpha_1$ (0.154 06-nm wavelength) radiation. Thicknesses were verified using x-ray reflectivity measurements using the same system (see Supplemental Material [36] for x-ray reflectivity data and the modeling used to determine sample thickness). Scanning electron microscopy (SEM) was performed using an Apreo SEM from Thermo Scientific and conducting probe atomic force microscopy (CPAFM) was performed using an Asylum Research Cypher AFM.

The electrical resistivity was measured in a tube furnace in the temperature range of room temperature to near T_{MIT} under a vacuum of $\sim 10^{-5}$ Torr using a four-probe technique. Parallel Pt contacts with 1 mm separation were deposited on top of the film by electron beam evaporation of 30 nm platinum in a molecular beam epitaxy (MBE) chamber. The lateral sample dimension used was approximately 10 mm × 5 mm. Samples were placed on the top of an alumina rod and a K-type thermocouple was affixed to the bottom side of the rod. Pt wires were pressed directly onto the contact pad using an alumina plate to avoid contact material contamination. The sample was placed in the center of the tube and heated at a rate of 5 K/min. The source current used was in the range of $10^{-5} - 10^{-6}$ A, and the output voltage was measured using a Keithley 2400 multimeter. The current was reversed for each measurement and the resistivity was calculated assuming a homogeneous current flow across the entire area of the film.

III. RESULTS AND DISCUSSION

NbO_2 thin films with a thickness ranging from 3.9 to 63.6 nm were grown using pulsed laser deposition on $Al_2O_3(0001)$ substrates. Reflection high-energy electron diffraction (RHEED) performed *in situ* immediately after film growth demonstrated epitaxial growth (see Fig. S1, Supplemental Material [36]). Atomic force microscopy showed that the surface roughness of the films was less than 1 nm (see Fig. S2, Supplemental Material [36]). Out-of-plane $\theta - 2\theta$ x-ray diffraction scans from as-grown films [Fig. 1(a)] showed only NbO_2 peaks with growth along the [110] crystallographic direction in terms of low-temperature tetragonal representation (see Fig. S3, Supplemental Material [36], for full-range scans). The crystal structure of the tetragonal phase is shown in Fig. 1(b). For thicker films, the $(440)_T$ reflection peak was positioned near the bulk value ($2\theta_{bulk} = 37.1°$, represented by the solid vertical line) [21]. The 63.6-nm film, which was grown at a lower growth rate than other samples, had an asymmetric peak with the main peak shifted toward a higher angle than the bulk because of the presence of a thicker strained layer in the film. The shift in the peak position, and thus the epitaxial strain, therefore depended not only on film thickness but also on the growth conditions. As discussed in more detail below, the asymmetry is due to a secondary broader peak corresponding to an unstrained, disordered layer with a lattice constant similar to that of the bulk material. The position of the peak of the 3.9-nm ultrathin film is represented by the dotted vertical line in Fig. 1(a). The shift is equivalent to a −1.1% compression in the out-of-plane lattice parameter. Film thickness, the a_T-lattice parameter, and growth conditions of all of the samples are listed in Table I.

Rocking curves from the $NbO_2(440)_T$ Bragg peaks for 63.6-, 15.6-, and 3.9-nm films are shown in Fig. 1(c). Films with a thickness ⩾15 nm depicted a double-peak structure: A fit using two Gaussian peaks yielded a sharp peak [full width at half maximum (FWHM) <0.1°, which was resolution-limited by the instrument] and a broad peak, both centered at

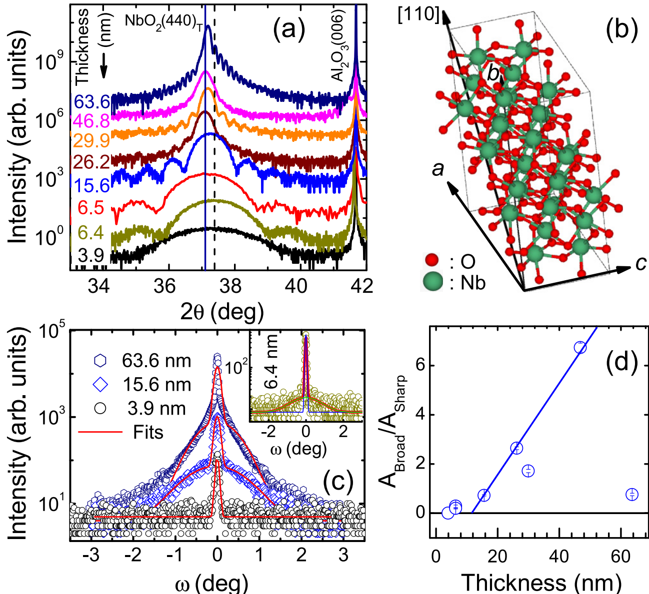

FIG. 1. Structural analysis. (a) X-ray diffraction (XRD) measured on the as-grown films. Scans around $NbO_2(440)_T$ only are presented, for clarity. The vertical solid and dashed lines represent the bulk-peak position and the peak position of the ultrathin film, respectively. (b) The crystal structure of the tetragonal NbO_2 phase. The growth direction is represented by an arrow labeled with [110]. (c) Rocking curves of $NbO_2(440)_T$ peaks. Films thicker than 15 nm showed a clear two-peak structure. (d) Ratio of the fitted broad- to sharp-peak area vs film thickness with a linear fit to all samples grown under similar conditions (solid line).

TABLE I. List of samples with sample thickness, lattice parameters, and growth conditions used in this work.

Film thickness		a_T-Lattice parameter	Growth condition		
			Growth pressure	Ambient gas	Growth rate
(nm)	(unit cells)	(nm)	(mTorr)	($\%O_2/\%Ar$)	(nm/pulse)
3.9	4	1.354	0.1	100/0	0.8×10^{-3}
6.4	7	1.355	0.1	100/0	0.6×10^{-3}
6.5	7	1.355	2	1/99	0.9×10^{-3}
15.6	16	1.363	2	1/99	1.6×10^{-3}
26.5	27	1.370	2	1/99	1.3×10^{-3}
29.9	31	1.370	2	1/99	1.0×10^{-3}
46.8	48	1.369	2	1/99	1.2×10^{-3}
63.6	66	1.366	0.1	1/99	0.9×10^{-3}

similar positions, indicating the presence of two film phases with different concentrations of crystalline defects (data for all films may be found in Fig. S4 in the Supplemental Material [36]). The ratio of broad- to sharp-peak areas is shown in Fig. 1(d). From the decreasing broad-peak area with decreasing film thickness, we confirmed that the broad-peak component corresponded to a defect-rich film layer near the surface of the film, while the sharp component corresponded to the portion of the film closest to the substrate interface with relatively fewer structural defects. Also, extrapolation to the linear fit of broad- to sharp-peak ratio as a function of film thickness for films grown under identical conditions [Fig. 1(d)] indicated that the broad peak vanished near a critical thickness of ~12 nm. Two of the films, with thicknesses of 63.6 and 29.9 nm, did not fit into the trend, indicating that the broad- to sharp-peak ratio is affected by extrinsic defect states induced by different growth conditions. Those two films were grown at a slower rate than the others (0.9×10^{-3} nm/pulse for 63.6-nm film vs 1.2×10^{-3} nm/pulse for 46.8-nm film, for example), as listed in Table I. Thus, the strained layer thickness can be adjusted by using appropriate growth parameters. Two of the thinner films, having thicknesses of 6.4 and 6.5 nm, had a very small remnant of broad-peak features [Fig. 1(c), inset]. Only the thinnest film (3.9 nm) had a single sharp-peak structure, indicating the absence of the textured crystalline structure.

For further characterization of the strained layers, in-plane x-ray diffraction of 63.6- and 6.4-nm films was performed (Fig. 2). Figure 2(d) shows peaks from $(400)_T$ and $(222)_T$ reflections. The $(400)_T$ peaks from both films were found at the bulk position ($2\theta = 26.07^\circ$), indicating that part of the out-of-plane compression was compensated by in-plane expansion perpendicular to the crystallographic $[100]_T$ c axis as shown in Fig. 2(a). The $(222)_T$ peak of the 6.4-nm film, which is composed of a linear combination of the out-of-plane [110] and in-plane [001] lattice constants, was shifted toward a lower angular position by $\Delta(2\theta) \approx -0.17^\circ$ with respect to the 63.6-nm film. Using the d_{110} spacing from the out-of-plane measurement, we determined that the in-plane c-axis lattice parameter of the thinner film increased by 0.95% with respect to the 63.6-nm film. Using prior work on VO_2 [32–35], a schematic of the modification in the energy band due to the strain-induced atomic displacement along the c axis is illustrated in Fig. 2(b). The separation of e_g^π bands was enhanced by the tensile strain, causing an upward shift of the $e_g^{\pi^*}$ band from the Fermi level (E_F). Figure 2(e) shows the in-plane Φ scan of the $NbO_2(400)_T$ reflection measured for the 6.4-nm

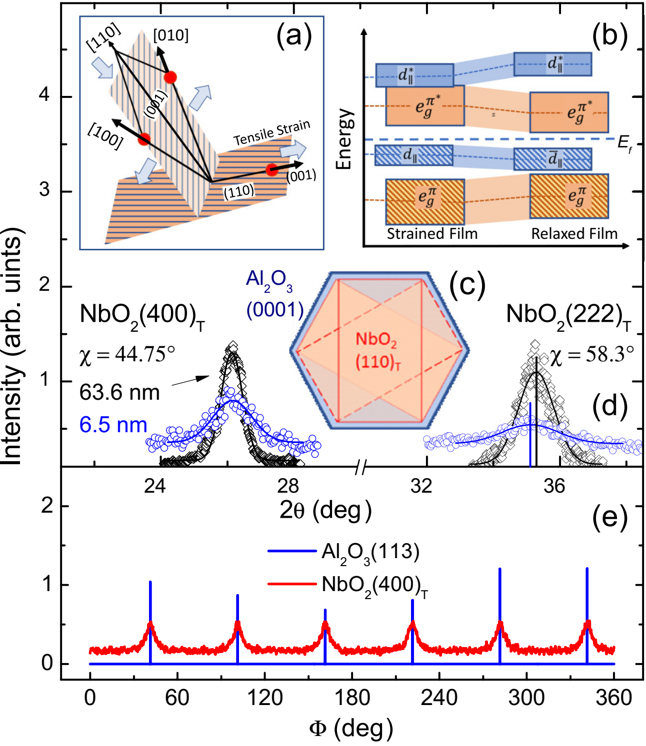

FIG. 2. In-plane x-ray diffraction and epitaxial strain model. (a) A schematic of the epitaxial compressing strain acting in the $(110)_T$ plane and resulting tensile strain along the $[001]_T$ direction of the NbO_2 crystal (not drawn to scale). (b) An estimation of the band structure in the strained and unstrained films (not drawn to scale). (d) In-plane θ-2θ scans from $(400)_T$ and $(222)_T$ reflections measured from a thin (6.4-nm) and 63.6-nm film showing a shift in the (222) peak position of the thinner film by 0.2° with respect to the thicker film. (e) In-plane Φ scans of $NbO_2(400)_T$ and $Al_2O_3(113)$ reflections measured from a 6.4-nm film. The film showed sixfold rotation symmetry due to the three mutually rotated in-plane twin domains as illustrated in (c).

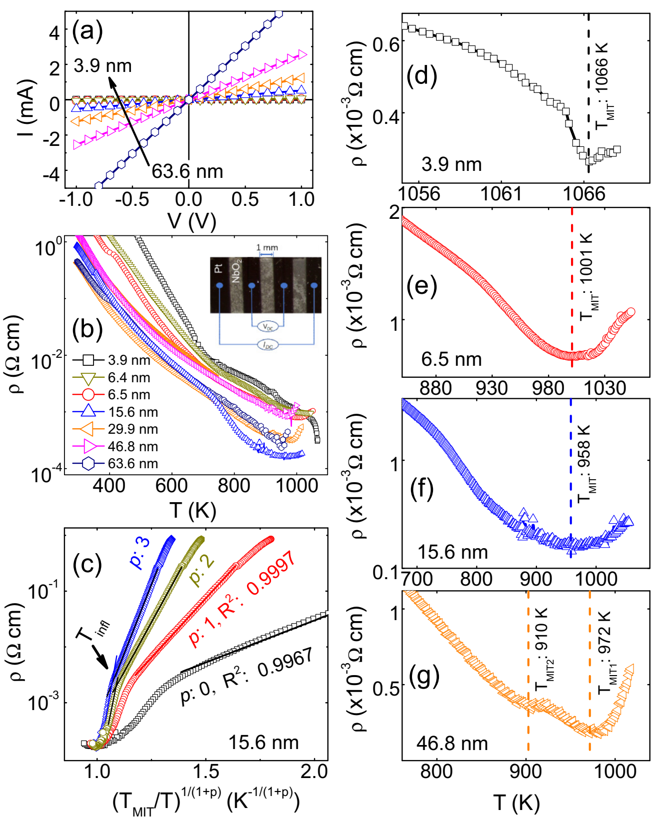

FIG. 3. Temperature-dependent resistivity. (a) The current-voltage characteristics of the Ohmic contacts. (b) The resistivity vs T measured using a four-probe technique. Inset: the sample image and measurement schematics. (c) A plot of resistivity vs $(10^3/T)^{1/(1+p)}$ of the 15.6-nm-thick film for thermal activation ($p = 0$), Efros-Shklovskii ($p = 1$), 2D Mott ($p = 2$), and 3D Mott ($p = 4$) conductivity models. Resistivity vs T data near T_{MIT} for (d) 3.9-, (e) 6.5-, (f) 15.6-, and (g) 46.8-nm films.

film overlaid with the (113) reflection of the substrate. The sixfold symmetry of the scan indicates the presence of three in-plane twin domains of the film [Fig. 2(c)], as expected in epitaxial films grown on $Al_2O_3(0001)$ [14,37,38]. Therefore, the c axis of the film, along which the metallic $d_{\|}$ bands [35] have a sixfold rotation symmetry in the plane of the film which removes the expected in-plane anisotropy in the conductivity.

The electrical resistivity was measured in a tube furnace from room temperature to near T_{MIT} under vacuum with a pressure of $\sim 10^{-5}$ Torr using a four-probe technique. All four Pt wires were pressed directly on Pt-contact pads [Fig. 3(b), inset] which avoided using contact materials. Two-terminal current-voltage cycles measured from -1 to $+1$ V [Fig. 3(a)] demonstrated Ohmic contact behavior. Figure 3(b) shows resistivity (ρ) vs temperature (T) data measured between room temperature and $T \sim 1100$ K. From room temperature to ~ 800 K, ρ decreased by more than four orders of magnitude. This low-temperature insulating-state conductivity did not follow an Arrhenius law [see $p = 0$ plot in Fig. 3(c) for the 15.6-nm film]. The data were better fitted using a $\log(\rho) = AT^{-(1+p)}$ power law, where $p = 1$ represents Efros-Shklovskii (ES) variable-range hopping (VRH) conduction [39] and $p = 2, 3$ represent the 2D and 3D Mott VRH conduction mechanisms [40], respectively. The data more closely matched the Mott or ES conduction based on these R^2 values obtained from the fits, but it was difficult to distinguish whether the Mott and ES mechanisms best fit the data. Mott conduction is likely dominant because ES conduction depends on a Coulomb gap that would presumably be insignificant at the high temperatures at which the samples were measured. The room temperature resistivity of 15.6-nm and thicker films ranged from 0.4 to 1.4 Ω cm, which is comparable to previous reports [31,37,41]. The metallic-state resistivity was found to be 10^{-3}–10^{-4} Ω cm, with the value of 3×10^{-4} Ω cm being for the 3.9-nm film.

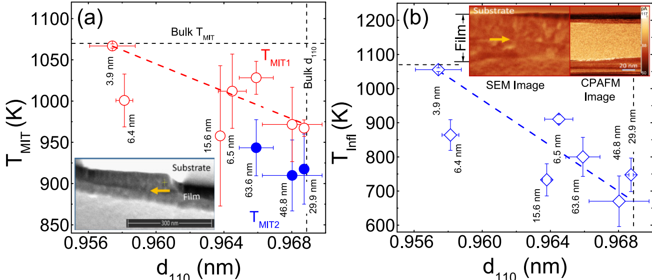

FIG. 4. Variation of transition temperature. (a) The metal-insulator transition temperature (T_{MIT}) as a function of out-of-plane spacing (d_{110}) showing a general increase in T_{MIT} with a decreasing d_{110} spacing. Horizontal and vertical dotted lines represent the bulk T_{MIT} and bulk d_{110}, respectively. Inset: SEM cross-sectional image of the 63.6-nm film. The interface between strained and relaxed layer is indicated by the yellow arrow. (b) T_{Infl} plotted as a function of d_{110}. Inset: On the left, a high-resolution cross-sectional SEM image of the interface, with the yellow arrow showing the boundary between the relaxed and strained layers. On the right, the conductive probe atomic force microscopy (CPAFM) image of the same film cross section showing a less conducting interface and the bulk layer with larger conductivity.

The thinnest film showed a sharp transition near the bulk transition temperature [Fig. 3(d)] as expected from the strained single-layer film. With increasing film thickness, the transition broadened [Figs. 3(e) and 3(f) for the 6.5- and 15.6-nm-thick samples, respectively], finally splitting into double transitions, T_{MIT1} and T_{MIT2} for the thicker films, as shown in Fig. 3(g) for the 46.9-nm film. Presumably T_{MIT1}, which is higher than T_{MIT2}, was the transition temperature corresponding to the strained layer since it is similar to the transition temperatures of the thinner films which have a larger percentage of their thickness that is strained.

Figure 4 shows the dependence of the T_{MIT} [Fig. 4(a)] and inflection temperature (T_{Infl}) [Fig. 4(b)] on the (110) out-of-plane lattice constant d_{110}. The T_{MIT} was determined as the temperature at the minima of the inverse Gaussian fit where the actual metallic behavior appeared, while T_{Infl} was determined from the intersection of two slopes before and after the inflection in the resistivity, as shown in Fig. 3(c). According to Goodenough [34], the pairing of Nb-Nb occurs below the temperature T_{Infl} while lattice distortion via octahedral rotations occurs near T_{MIT}. As the out-of-plane compression increased (d_{110} decreased), both T_{MIT} and T_{Infl} increased, as represented by the linear fits (dotted lines) in Fig. 4.

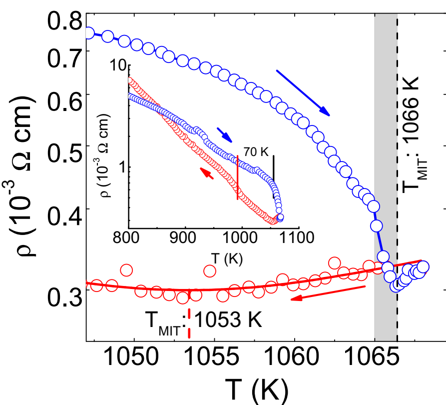

FIG. 5. Metal-to-insulator transition in an ultrathin film. Metal-to-insulator transition in a 3.9-nm film during heating and cooling, indicated by the arrowhead directions. The shaded region represents the sharp change in the resistivity due to the structural change and the dotted line represents the T_{MIT}. Inset: The figure replotted with a larger temperature range scale where the solid vertical lines represent the T_{Infl} during heating and cooling, showing a hysteresis of 70 K.

To verify the double-layered film structure, cross-sectional scanning electron microscopy (SEM) and conducting probe atomic force microscopy (CPAFM) were performed on the 63.6-nm film (insets, Fig. 4). The cross-sectional SEM image showed a bottom layer with highly textured features and a top relaxed layer with a distinct interface between them (indicated by the arrow). The ratio of the thicknesses of the strained layer and relaxed layer was consistent with the ratio of broad to sharp x-ray rocking curve peaks in Fig. 1(d), verifying our hypothesis of a two-layer film structure. The inset of Fig. 4(b) shows the combined SEM and CPAFM images. No clear distinction between the relaxed and strained layer in CPAFM was observed, indicating that a sharp contrast in conductivity between the two layers was not present.

The ultrathin film showed the sharpest metal-to-insulator transition. The temperature-dependent resistivity data for the 3.9-nm-thick film in the high-temperature region are shown in Fig. 5. From the rocking curve in Fig. 1(c), this film had a single-peak structure, indicating a complete absence of the textured layer with a 1.2% compressive strain along the $[100]_T$ and $[010]_T$ directions. This film also had a $T_{\mathrm{Infl}} = 1058$ K and a sharp metal-to-insulator transition at $T_{\mathrm{MIT}} = 1066$ K, followed by a linear increase in resistivity with increasing temperature, indicating a distinct metallic behavior above T_{MIT}. Below the abrupt metal-to-insulator transition, there was a gradual transition near 1063 K due to the coexistence of insulator and metallic phases, consistent with a similar VO_2 transition caused by a local structural deformation [42]. The feature might also arise from the surface-strain state or from the segregation of electronic-type (Mott) and structural-type (Peierls) transitions. During cooling, T_{MIT} was 1053 K, nearly 13 K lower than the T_{MIT} while heating. The T_{Infl} during cooling was 960 K, yielding a hysteresis of 70 K.

Due to the presence of a strained layer, a relaxed layer, and interfaces, which act as parallel channels with different conductivities, the resultant room temperature resistivity of the thicker films was lower than in ultrathin films. Thicker films showed double transitions corresponding to the strained and relaxed layers, with the larger transition temperature T_{MIT1} corresponding to the strained layer. The film having a thickness of 3.9 nm, which had a single sharp rocking curve, only had the fully strained layer. As a result, the resistivity in this ultrathin film showed a sharp transition with T_{MIT} near the bulk transition temperature. The structural phase transition (shaded region in Fig. 5) and electronic (MIT) transition (dotted line in Fig. 5) occurred simultaneously within a small temperature difference of 2 K. The phase transition in this NbO_2 thin film was first order because of the presence of the sharp discontinuity in resistivity and the large thermal hysteresis near the transition temperature. In the literature, the transition is claimed to be first order by some groups [27,43] and second order by others [22,24,28]. Rao *et al.* found the evidence of thermal hysteresis of 8 K using differential thermal analysis (DTA) studies [27]. They measured approximately 600 J/mole of enthalpy change during the phase transition. Sakata *et al.* found a discontinuity in thermal expansion near the transition temperature signifying the transition was first order in nature [19]. Shapiro *et al.*, in contrast, did not observe a discontinuity nor a thermal hysteresis in their neutron scattering studies and thus claimed a second-order transition [22].

The increasing trend of T_{MIT} and T_{Infl} with a decreasing out-of-plane d_{110} lattice constant can be explained in terms of the defect density present in the films. Thicker films acted as a bilayer structure, with two distinct layers with different defect densities resulting in a double transition. It is possible that the strained layer had more defects as the strained layer thickness increased, therefore lowering the transition temperature. On the other hand, the higher T_{MIT} in the thinnest film can be ascribed to the increased tensile strain which induced atomic displacements along the c axis. The atomic displacements, in turn, decreased apical Nb-O distances and increased the metal-oxide band overlap, ultimately shifting the $e_g^{\pi^*}$ energy band above the Fermi level, thus enhancing the stability of the insulating state [35,33]. It is, however, not possible to prove which of these two mechanisms, the vacancy model or the strain-induced band energy model, is dominant because the thinnest film, with the least number of defects, had a T_{MIT} similar to that of bulk NbO_2. A clear enhancement of T_{MIT} above the bulk value would certainly prove that the energy band modification model solely played the role in the transition temperature modulation, but this was not observed. On the other hand, if the transition temperature is expected to decrease in ultrathin films due to a crossover to a quasi-two-dimensional system, it is remarkable that the transition temperature of the 3.9-nm film is the same as the bulk material, which would illustrate the importance of the epitaxy-induced strain.

IV. CONCLUSIONS

We have measured the temperature-dependent resistivity and metal-to-insulator transition in epitaxial thin films of NbO_2 with thicknesses ranging from 3.9 to 63.6 nm synthesized on $Al_2O_3(0001)$ substrates using pulsed laser deposition. X-ray diffraction revealed an out-of-plane

compression which yielded an extension along the in-plane c- and $c_{\perp}$-crystallographic axes with decreased film thickness. The temperature-dependent resistivity in thicker films showed double transitions with different transition temperatures, T_{MIT1} and T_{MIT2}, due to the existence of a strained ordered layer and a relaxed disordered layer that have different defect densities. The transition temperature (T_{MIT}) increased with a decreasing out-of-plane lattice constant d_{110}. The ultrathin 3.9-nm film showed a first-order phase transition at 1066 K which is similar to that of the bulk material. The sharp bulklike transition in the ultrathin film is due to the presence of a single strained layer with minimum defect density.

ACKNOWLEDGMENTS

This work is supported by the University of California Multicampus Research Programs and Initiatives Grant No. MRP–17-454963. We acknowledge the help of Brandon Cheney at UC Santa Cruz for performing SEM imaging.

[1] M. D. Pickett, G. Medeiros-Ribeiro, and R. S. Williams, A scalable neuristor built with Mott memristors, Nat. Mater. **12**, 114 (2012).

[2] J. C. Shank, M B. Tellekamp, M. J. Wahila, S. Howard, A. S. Weidenbach, B. Zivasatienraj, L. F. J. Piper, and W. A. Doolittle, Scalable memdiodes exhibiting rectification and hysteresis for neuromorphic computing, Sci. Rep. **8**, 12935 (2018).

[3] K. Moon, E. Cha, J. Park, S. Gi, M. Chu, K. Baek, B. Lee, S. Oh, and H. Hwang, High density neuromorphic system with $Mo/Pr_{0.7}Ca_{0.3}MnO_3$ synapse and NbO_2 IMT oscillator neuron, in *Proceedings of the 2015 IEEE International Electron Devices Meeting* (IEEE, Piscataway, NJ, 2015), pp. 17.6.1–17.6.4.

[4] D. Lee, E. Cha, J. Park, C. Sung, K. Moon, S. A. Chekol, and H. Hwang, NbO_2-based frequency storable coupled oscillators for associative memory application, IEEE J. Electron. Devices Soc. **6**, 250 (2018).

[5] S. Kim, J. Park, J. Woo, C. Cho, W. Lee, J. Shin, G. Choi, S. Park, D. Lee, B. H. Lee, and H. Hwang, Threshold switching characteristics of a nanothin-NbO_2-layer-based $Pt/NbO_2/Pt$ stack for use in cross-point-type resistive memories, Microelectron. Eng. **107**, 33 (2013).

[6] X. Liu, S. M. Sadaf, M. Son, J. Shin, J. Park, J. Lee, S. Park, and H. Hwang, Diode-less bilayer oxide ($WO_x - NbO_x$) device for cross-point resistive memory applications, Nanotechnology **22**, 475702 (2011).

[7] E. Cha, J. Park, J. Woo, D. Lee, A. Prakash, and H. Hwang, Comprehensive scaling study of NbO_2 insulator-to-metal-transition selector for cross point array application, Appl. Phys. Lett. **108**, 153502 (2016).

[8] E. Cha, J. Woo, D. Lee, S. Lee, J. Song, Y. Koo, J. Lee, C. Park, M. Yang, K. Kamiya, K. Shiraishi, B. Magyari-Kope, Y. Nishi, and H. Hwang, Nanoscale (∼10 nm) 3D vertical ReRAM and NbO_2 threshold selector with TiN electrode, in *Proceedings of the 2013 IEEE International Electron Devices Meeting* (IEEE, Piscataway, NJ, 2013), pp. 10.5.1–10.5.4.

[9] R. Waser and M. Aono, Nanoionics-based resistive switching memories, Nat. Mater. **6**, 833 (2007).

[10] S. H. Chang, S. B. Lee, D. Y. Jeon, S. J. Park, G. T. Kim, S. M. Yang, S. C. Chae, H. K. Yoo, B. S. Kang, M. J. Lee, and T. W. Noh, Oxide double-layer nanocrossbar for ultrahigh-density bipolar resistive memory, Adv. Mater. **23**, 4063 (2011).

[11] L. Chua, Resistance switching memories are memristors, Appl. Phys. A **102**, 765 (2011).

[12] J. Park, T. Hadamek, A. B. Posadas, E. Cha, A. A. Demkov, and H. Hwang, Multi-layered $NiO_y/NbO_x/NiO_y$ fast drift-free threshold switch with high I_{on}/I_{off} ratio for selector application, Sci. Rep. **7**, 6018 (2017).

[13] X. Liu, S. K. Nandi, D. K. Venkatachalam, K. Belay, S. Song, and G. Elliman, Reduced threshold current in NbO_2 selector by engineering device structure, IEEE Electron. Device Lett. **35**, 1055 (2014).

[14] T. Joshi, T. R. Senty, R. Trappen, J. Zhou, S. Chen, P. Ferrari, P. Borisov, X. Song, M. B. Holcomb, A. D. Bristow *et al.*, Structural and magnetic properties of epitaxial delafossite CuFeO2 thin films grown by pulsed laser deposition, J. Phys. D: Appl. Phys. **117**, 013908 (2015).

[15] T. Joshi, P. Borisov, and D. Lederman, The role of defects in the electrical properties of NbO_2 thin films vertical devices, AIP Adv. **6**, 125006 (2016).

[16] T. Joshi, P. Borisov, and D. Lederman, Structural and electrical characterization of polycrystalline NbO_2 thin film vertical devices grown on TiN-coated SiO_2/Si substrate, J. Appl. Phys. **124**, 114502 (2018).

[17] Y. Wang, R. B. Comes, S. A. Wolf, and J. Lu, Threshold switching characteristics of $Nb/NbO_2/TiN$ vertical devices, IEEE J. Electron Devices Soc. **4**, 11 (2016).

[18] G. Belanger, J. Destry, G. Perluzzo, and P. M. Raccah, Electron transport in single crystals of niobium oxide, Can. J. Phys. **52**, 2272 (1974).

[19] T. Sakata, K. Sakata, and I. Nishida, Study of phase transition in NbO_2, Phys. Status Solidi **20**, K155 (1967).

[20] K. J. Sakata, Study of the phase transition in $Nb_xTi_{1-x}O_2$, J. Phys. Soc. Jpn. **26**, 582 (1969).

[21] A. A. Bolzan, C. Fong, and B. J. Kennedy, A powder neutron diffraction study of semiconducting and metallic niobium oxide, J. Solid State Chem. **113**, 9 (1994).

[22] S. M. Shapiro, J. D. Axe, G. Shirane, and P. M. Raccah, Neutron scattering study of the structural phase transition in NbO_2, Solid State Commun. **15**, 377 (1974).

[23] V. Eyert, The metal-insulator transitions of VO_2: A band theoretical approach, Ann. Phys. (Leipzig) **11**, 650 (2002).

[24] A. O'Hara and A. A. Demkov, Nature of the metal-insulator transition in NbO_2, Phys. Rev. B **91**, 094305 (2015).

[25] G. Brauer, Die oxide des niobs, Z. Anorg. Chem. **248**, 1 (1941).

[26] R. F. Janninck and D. H. Whitmore, Electrical conductivity and thermoelectric power of niobium oxide, J. Phys. Chem. Solids. **27**, 1183 (1966).

[27] C. N. R. Rao, G. R. Rao, and G. V. S. Rao, Semiconductor-metal transition in NbO_2 and $Nb_{1-x}V_xO_2$, Solid State Chem. **6**, 340 (1972).

[28] K. Seta and L. Naito, Calorimetric study of the phase transition in NbO_2, J. Chem. Thermodyn. **14**, 921 (1982).

[29] K. Sakata, Note on the phase transition in NbO_2, J. Phys. Soc. Jpn. **26**, 1067 (1969).

[30] S. H. Shin, T. Halpern, and P. M. Raccah, High-speed high-current field switching of NbO_2, J. Appl. Phys. **48**, 3150 (1977).

[31] F. J. Wong, N. Hong, and S. Ramanathan, Orbital splitting and optical conductivity of the insulating state of NbO_2, Phys. Rev. B **90**, 115135 (2014).

[32] L. L. Fan, S. Chen, Z. L. Luo, Q. H. Liu, Y. F. Wu, L. Song, D. X. Ji, P. Wang, W. S. Chu, C. Gao, C. W. Zou, and Z. Y. Wu, Dynamics of ultrathin VO_2 film grown on TiO_2 (001) and associated phase transition modulation, Nano Lett. **14**, 4036 (2014).

[33] N. B. Aetukuri, A. X. Gray, M. Drouard, M. Cossale, L. Gao, A. H. Reid, R. Kukreja, H. Ohldag, C. A. Jenkins, E. Arenholz, K. P. Roche, H. A. Durr, M. G. Samant, and S. S. P. Parkin, Control of metal-to-insulator transition in vanadium dioxide by modifying orbital occupancy, Nat. Phys. **9**, 661 (2013).

[34] J. B. Goodenough, The two components of the crystallographic transition in VO_2, J. Solid State Chem. **3**, 490 (1971).

[35] J. B. Goodenough, Direct cation-cation interactions in several oxides, Phys. Rev. **117**, 1442 (1960).

[36] See Supplemental Material at http://link.aps.org/supplemental/10.1103/PhysRevMaterials.3.124602 for reflection high-energy electron diffraction (RHEED) images, atomic force microscopy (AFM) images, and x-ray diffraction (XRD) and x-ray reflectivity (XRR) data.

[37] Y. Wang, R. B. Comes, S. Kittiwatanakul, S. A. Wolf, and J. Lu, Epitaxial niobium dioxide thin films by reactive-biased target ion beam deposition, J. Vac. Sci. Technol. A **33**, 021516 (2015).

[38] F. Wong and S. Ramanathan, Heteroepitaxy of distorted rutile-structure WO_2 and NbO_2 thin films, J. Mater. Res. **28**, 2555 (2013).

[39] A. L. Efros and B. I. Shklovskii, Coulomb gap and low temperature conductivity of disordered system, J. Phys. C: Solid State Phys. **8**, L49 (1975).

[40] N. F. Mott, Metal-insulator transition, Rev. Mod. Phys. **40**, 677 (1968).

[41] L. Noskin, H. A. Seidner, and D. Schlom, Growth of NbO_2 by molecular-beam epitaxy and characterization of its metal-to-insulator transition, MRS Adv. **2**, 3031 (2017).

[42] J. I. Sohn, H. J. Joo, D. Ahn, H. H. Lee, A. E. Porter, K. Kim, D. J. Kang, and M. E. Welland, Surface-stress induced transition and nature of associated special phase transition in single crystalline VO_2 nanowires, Nano Lett. **9**, 3392 (2009).

[43] K. T. Jacob, C. Shekhar, and M. Vinay, Thermodynamic properties of niobium oxides, J. Chem. Eng. Data **55**, 4854 (2010).